Energy Storage and Conversion 2024, 2(2), 369.
https://doi.org/10.59400/esc.v2i2.369

Article

Nitrided copper-iron composite oxides derived from layered double hydroxides for enhanced carbon dioxide electroreduction to methane and formic acid

Dian Song[1], Jinqing He[1], Yiping Wang[1,2,*], Xuhui Zhao[1], Fazhi Zhang[1], Xiaodong Lei[1,2,*]

[1] State Key Laboratory of Chemical Resource Engineering, Beijing University of Chemical Technology, Beijing 100029, China
[2] Quzhou Institute for Innovation in Resource Chemical Engineering, Quzhou 324000, Zhejiang Province, China
*** Corresponding authors:** Yiping Wang, wangyiping@buct.edu.cn; Xiaodong Lei, leixd@mail.buct.edu.cn

CITATION

Song D, He J, Wang Y, et al. Nitrided copper-iron composite oxides derived from layered double hydroxides for enhanced carbon dioxide electroreduction to methane and formic acid. Energy Storage and Conversion. 2024; 2(2): 369. https://doi.org/10.59400/esc.v2i2.369

ARTICLE INFO

Received: 27 November 2023
Accepted: 8 January 2024
Available online: 8 May 2024

Abstract: The reduction of carbon dioxide into valuable chemical products is a promising solution to address carbon balance and energy issues. Herein, amorphous nitrided copper-iron oxides are prepared by gas-phase nitriding of CuFe-layered double hydroxide precursors with urea as a nitrogen source. The obtained materials show high activity for CO_2 electroreduction to methane and formic acid, achieving a total Faraday efficiency of 74.7% at −0.7 V vs. RHE and exhibiting continuous 10 h durability in the H-cell. The uniformly distributed Cu+ sites act as active sites by losing electrons to activate CO_2. During the CO_2 electroreduction, CO_2 is converted to *COOH via proton-electron coupling; *COOH combines directly with a proton in solution to produce the HCOOH product; and the other part of *COOH undergoes a protonated dehydration process to form the *CHO intermediate, which dehydrates again to form CH_4. This study provides a new approach for designing CO_2 electroreduction catalysts.

Keywords: CuFe-LDH; nitrided copper-iron oxides; CO_2 electroreduction; electrocatalysis

1. Introduction

Carbon dioxide (CO_2) is a key contributor to the global warming crisis in modern-day society. Excessive emissions of CO_2 have resulted in severe environmental issues, including the greenhouse effect, acidification of water bodies, and climate change. These challenges present a significant threat to the sustainable development of society [1]. The combustion of fossil fuels from anthropogenic sources is the major source of atmospheric CO_2 emissions [2]. The main ways to achieve zero CO_2 emissions are through the decarbonization of raw materials, carbon sequestration and capture, as well as carbon recovery and neutralization [3–5]. The most efficient method for converting CO_2 into valuable chemicals today is electrocatalytic reduction [6,7]. However, the electrocatalytic reduction of CO_2 faces challenges such as the hydrogen evolution reaction (HER) competing with the desired reaction [8]. Additionally, the highly thermodynamic stability and kinetic inhibitory effects of CO_2 molecules result in their deactivation [9,10]. Therefore, the top priority in research in electrocatalytic reduction of carbon dioxide is to design catalysts with low overpotential that can suppress the HER and effectively promote the reduction of carbon dioxide. These catalysts should also possess advantages such as low cost, high selectivity, stability, and durability.

Due to limited reserves and high costs of precious metals, transition metals with significant stability and high economic feasibility in alkaline media have attracted considerable attention in the field of electrocatalysis [11]. Therefore, it is necessary to

search for transition metal catalysts with higher catalytic activity [12–14]. Iron-based materials are considered to be very promising catalysts due to their low cost and environmental friendliness [15]. However, iron-based materials continue to face a significant challenge in terms of low conductivity [16], limiting their electrocatalytic performance. The reduction intermediate CO in the carbon dioxide is harmful to iron-based materials because CO can damage the active sites of iron-based catalysts., further limiting their effectiveness in electrocatalysis [17]. Scientists are now extensively overcoming this limitation by coupling iron-based materials with other materials such as metal oxides or organic carbon frameworks [18,19]. Copper-based catalysts have garnered significant research attention due to their high efficiency in converting carbon dioxide into hydrocarbons [20,21]. In recent years, considerable research has been conducted with the aim of designing efficient Cu-based heterogeneous materials as Carbon Dioxide Reduction Reaction (CO_2RR) electrocatalysts. These materials include monometallic Cu, Cu-based oxides, Cu-based bimetallic systems, single/dual Cu atoms, and Cu-based metal-organic frameworks (MOFs) [22]. To improve the CO_2 reduction activity of catalysts, structural adaptations such as modification of active sites, morphology or size [23,24], introducing other elements [25,26], as well as surface modification and electroplating [27–29] are being investigated. Among of these methods, nitrides of transition metals exhibit exceptional electronic [30–32], mechanical and optical properties, making them very suitable for reducing CO_2 to C_1 products [32–35]. Nitrides of transition metals are usually solid compounds with strong metal-nitrogen bonds [36], which gives them a high degree of structural stability. Compared to other catalysts, transition metal nitrides cause less corrosion or structural changes during electrochemical processes. Therefore, it can participate in the reaction stably for a long time [37]. Despite their high electrochemical activity, the limited number of electrochemically active sites in nitrides of transition metals may affect their catalytic efficiency in practical reactions [38]. Amorphous materials are rich in active defect sites, thus favoring efficient CO_2 electroreduction. Shan et al. synthesized Cu@CuEu nanoparticles with amorphous CuEu alloy shells. Defect sites in the amorphous material, which may interact effectively with CO_2 molecules or their reduction intermediates, optimize the reaction pathway for CO_2 reduction [39]. Yang et al. prepared Bi-based catalysts with amorphous layers. The disordered arrangement of atoms in the amorphous materials provides more CO_2 adsorption sites and may reduce the activation energy of CO_2 molecules by changing the electronic structure of the catalysts. This facilitates the subsequent reduction steps [40].

The structural units of Layered Double Hydroxides (LDHs) primarily exhibit an octahedral geometry, where hydroxyl ions are situated at the vertices of the octahedron, and the encapsulated metal ions are positioned at the center. LDHs have a general chemical formula of $[M^{2+}_{1-x}M^{3+}_{x}(OH)_2]^{x+}(A^{n-})_{x/n}\cdot yH_2O$, in which M^{2+}, M^{3+}, and A respectively represent divalent cations (e.g., Ni^{2+}, Mg^{2+}, Cu^{2+}, Ca^{2+}), trivalent cations (e.g., Fe^{3+}, Al^{3+}), and anions [41]. By selecting different metals and anionic species, various types of LDHs can be synthesized. The high degree of design flexibility gives LDHs extensive potential applications in various catalytic reactions, such as photocatalysis, thermocatalysis, and electrocatalysis, including CO_2RR [42–44]. Ma et al. have demonstrated that Cd-MgAl-LDHs exhibit exceptional activity in

the electrochemical reduction of CO_2 to CO [45]. Zhang et al. found that $Cu_9Zn_1/Cu_{0.8}Zn_{0.2}Al_2O_4$ generated from CuZnAl-LDH enhanced the adsorption of CO intermediates and promoted C-C coupling, greatly improving the activity of CO_2RR [46].

Our group has previously demonstrated that CuFe-LDH could serve as an outstanding precursor for electrochemical catalysts due to its unique properties [47]. In this study, we successfully synthesized amorphous nitrided copper-iron oxides through the gas-phase nitridation of CuFe-LDH, exploiting the distinctive and highly dispersed metal components present in LDH. To understand the correlation between the material structure and the performance of CO_2RR, the chemical composition and the existence state of surface elements are analyzed, and the formed gas and liquid products of CO_2RR are detected. The reaction mechanism was studied through X-ray photoelectron spectroscopy (XPS), X-ray diffraction (XRD), and in situ attenuated total reflection fourier transform infrared spectroscopy (ATR-FTIR). The dispersion of copper in nanoparticles results in a highly uniform distribution, thereby enhancing its activity in the electroreduction of CO_2.

2. Experimental

2.1. Chemicals and materials

The chemical reagents used in this work include $Cu(NO_3)_2 \cdot 3H_2O$ (≥99.0%, Macklin), $Fe(NO_3)_3 \cdot 9H_2O$ (≥98.5%, Macklin), NaOH (≥96.0%, Tianjin Fuchen Chemical Reagents), $KHCO_3$ (≥99.0%, Aladdin), Na_2CO_3 (≥99.0%, Beijing Chemical Plant), and $CO(NH_2)_2$ (≥99.0%, Macklin). Deionized water was utilized in the experiment. Ar (≥99.999%), CO_2 (≥99.999%), and N_2 (≥99.999%) were purchased from Beijing Shunanqite Gas. All of the chemicals in this study were used without any additional purification.

2.2. Fabrication of nitrided copper-iron composite oxides

The CuFe-LDH precursor was prepared using the co-precipitation process. 0.0075 mol of $Cu(NO_3)_2 \cdot 3H_2O$ and 0.0025 mol of $Fe(NO_3)_3 \cdot 9H_2O$ were dissolved in 60 mL of deionized water. 0.02 mol of NaOH and 0.005 mol of Na_2CO_3 were dissolved in 60 mL of deionized water. The two solutions were added dropwise into a three-necked flask under continuous magnetic stirring, maintaining the pH of mixed solution at 5 in the above process. After addition, the mixed solution was stirred for one hour and transferred into a hydrothermal reactor for 5 h reaction at 110 ℃. After the completion of hydrothermal treatment, the obtained CuFe-LDH samples were collected through centrifugation, filtration and drying.

The nitrided copper-iron composite oxides were prepared by the gas-phase nitridation of CuFe-LDH precursors with urea as nitrogen source. 0.5 g CuFe-LDH sample and 5 g urea were transferred to tube furnace, then the nitridation reaction was conducted at 300 ℃ for 2 h with a heating rate of 1 $℃ \cdot min^{-1}$ in N_2. After the nitridation, the obtained sample was washed with ethanol, centrifuged, and vacuum dried.

2.3. Characterization

XRD patterns were acquired by a Bruker D8A25 instrument with Cu Kα radiation and a scanning step of $10°\cdot min^{-1}$. Scanning electron microscope (SEM) images were captured on a Zeiss SUPRA 55 instruments operated at 10 kV. High-resolution transmission electron microscopy (HRTEM) images were taken using a JEOL JEM-F200 instrument equipped with an energy dispersive X-ray spectrometer (EDS), and the test was conducted at an accelerating voltage of 200 kV. XPS and Cu LMM Auger spectra were acquired through a Thermo VG ESCALAB 250 X-ray photoelectron spectrometer with Al Kα X-rays at approximately 2×10^{-9} Pa. ATR-FTIR was conducted in situ using a Tensor II (Bruker) FTIR spectrometer with an MCT detector. The measurements were performed with a VeeMAX III variable angle specular reflection accessory (Pike, USA) and a spectroelectrochemical cell, combined with a CHI660E instrument to control the reduction potential. Gas chromatography (GC, Shimadzu, GC2014) at 20 ℃ was utilized to quantify gaseous product. The concentration of Cu and Fe in the material was determined using inductively coupled plasma mass spectrometry (ICP-MS, iCAP6300 Radial, Thermo, US).

2.4. Electrochemical study of CO_2 reduction and products analysis

Electrochemical measurements were performed using a CHI660E electrochemical workstation (Shanghai Chenhua Instruments Co., China) in a three-electrode system within an H-cell. The cathode and anode were separated by a Nafion 115 membrane, which acted as a proton exchange membrane. A 0.5 M $KHCO_3$ electrolyte was utilized for the measurements. The working, counter, and reference electrodes are nitrided copper-iron composite oxide powder, graphite rod, and Ag/AgCl (3 $mol\cdot L^{-1}$ KCl), respectively. The given potential was converted to a reversible hydrogen electrode (RHE) using the Nernst equation. The electrolyte that contained 0.5 M $KHCO_3$ saturated with CO_2 exhibited a pH of 7.12.

$$E_{V\ vs\ RHE} = E_{V\ vs\ Ag/AgCl} + (0.21 + 0.059 \times pH)\ V$$

During the linear sweep voltammetry (LSV) tests, CO_2 (≥99.999%) or Ar (≥99.999%) with high purity were continuously injected into the H-cell. The electrolyte was saturated with CO_2 at a mass flow rate of 30 $mL\cdot min^{-1}$ for over 20 min, following which the cell was hermetically sealed before executing the measurements. After each measurement that lasted for 1.5 h at various overpotentials, the formed products were analyzed.

3. Results and discussion

3.1. Structure of as-prepared catalysts

The XRD patterns of CuFe-LDH and nitrided copper-iron composite oxides are shown in **Figure 1a**. The spectrum of the CuFe-LDH precursor can observe diffraction peaks at 12.8°, 25.8°, 33.1°, 36.6°, 43.6°, 60.9°, and 62.5°, which are respectively attributed to the (003), (006), (009), (015), (018), (110), and (113) crystal faces of the LDH phase [48]. This indicates the successful synthesis of the hydrotalcite precursor. The XRD pattern of nitrided copper-iron composite oxides shows that there are no additional XRD signal peaks except for the C signal peak at 18° indexed to the

standard C (JCPDS No. 48-1449), confirming the amorphous nature of obtained material. Amorphous materials are more likely to produce defective vacancies during the reaction process, which can serve as active sites for catalytic reactions [49]. Furthermore, a detailed investigation of this composite was conducted by analyzing XPS spectra. (**Figures 1b** and **1c**). It is visible in the spectrum that peaks of Cu 2p at 932.37 and 952.38 eV correspond to zero valent Cu (Cu^0); in addition to that, Cu 2p at 932.37 and 953.38 eV peaks correspond to the Cu $2p_{3/2}$ and $2p_{1/2}$ (**Figure 1a**), but it cannot confirm that Cu^+ or Cu^0 coexist. They were analyzed in conjunction with the LMM spectrum of Cu (**Figure 1b**). The apparent appearance of a signal for Cu^+ [50]. So the presence of Cu^+ was established. Two peaks of Fe 2p at 709.20 and 714.6 eV are within the scope of the Fe $2p_{3/2}$ binding energy, corresponding to Fe^{2+} and Fe^{3+}, respectively (**Figure A1**), further confirms the existence of Fe^{2+} and Fe^{3+} in the composite. The overlapping of the $2P_{1/2}$ and $2P_{3/2}$ peaks of Fe could be due to the interference of the LMM spectrum of Cu. This suggests that charge rearrangement may have occurred within the material after nitriding, which may have led to increased conductivity of the material and enhanced electrochemical activity.

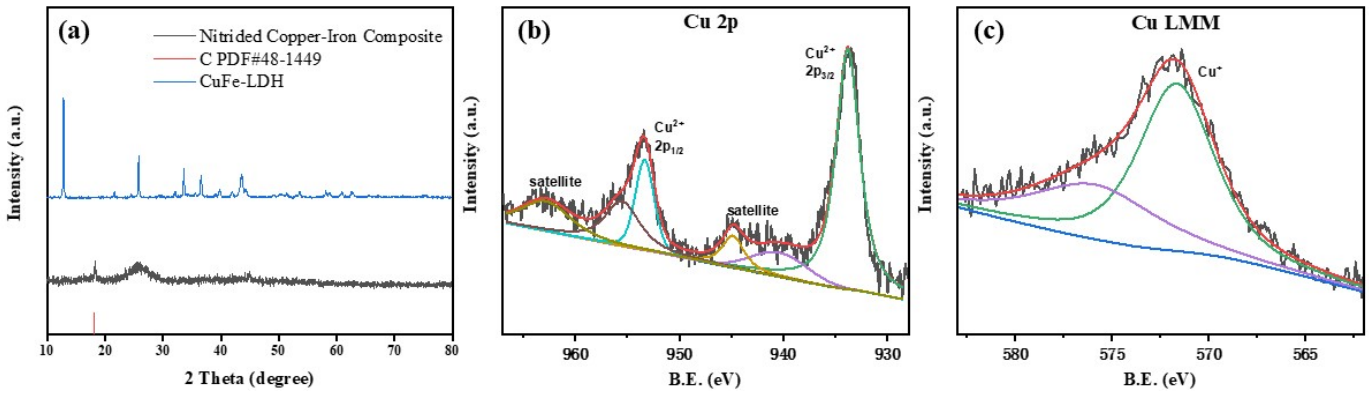

Figure 1. (a) XRD analyses of CuFe-LDH and nitrided copper-iron composite oxides; **(b)** XPS spectra of Cu 2p; **(c)** Cu LMM.

SEM images of CuFe-LDH (**Figure A2**) show that CuFe-LDH has a nanosheet morphology with a smooth surface and approximately 100 nm of thickness. After the nitriding reaction, the catalyst was transformed into nanoparticle with diameters ranging from 50 to 100 nm (as shown in **Figures 2a** and **2b**). The HRTEM image (**Figure 2h**) shows no lattice fringing detected, which was considered a typical characteristic of amorphous state [51]. This further supports an amorphous nature of nitrided copper-iron composite oxides. In addition, EDS elemental mapping (**Figures 2c–2g**) confirms the homogeneous distribution of Cu, Fe, O, and N atoms on the surface of the catalyst. The EDS results indicate that the elemental contents of Cu, Fe, N, and O are 47.6%, 14.59%, 17.44%, and 20.37%, respectively (**Figure A3**).

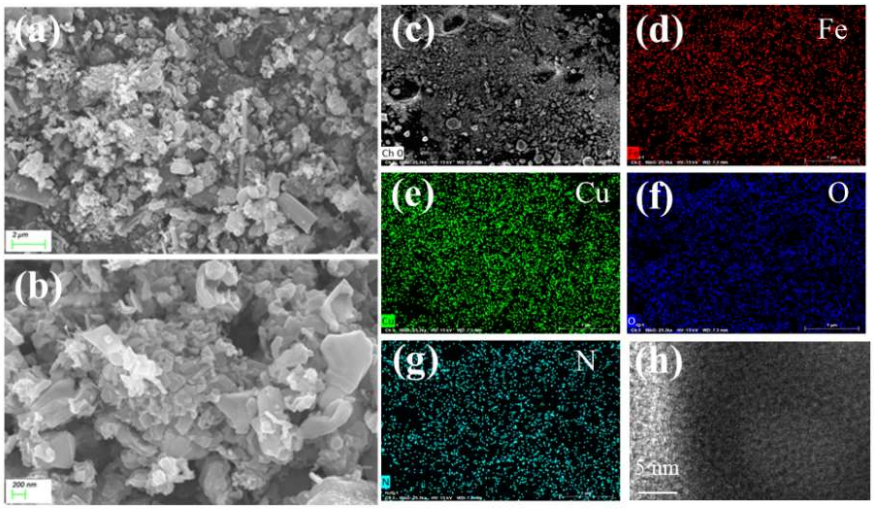

Figure 2. (a–b) SEM images of nitrided copper-iron composite oxides; **(c-g)** EDS mapping results; **(h)** HRTEM.

3.2. CO_2RR performance of as-prepared catalysts

The CO_2 electroreduction performance of nitrided copper-iron composite oxide was investigated in an H-type cell containing 0.5 M $KHCO_3$. **Figures 3a** and **3b** show the stable LSV curves of nitrided copper-iron composite oxide and CuFe-LDH in Ar-saturated (dashed line) and CO_2-saturated (solid line) electrolytes, respectively. The current density of the catalyst is significantly lower than that of the precursor at the same overpotential. As shown in **Figures 3a** and **3b**, the current density remained stable with the increase of overpotential, suggesting that the catalyst did not fall off throughout the reaction process. Moreover, there was no significant fluctuation in the current density during the test (**Figure 3c**), indicating the high stability of the catalyst. In the CO_2 atmosphere, the catalyst exhibits a lower initial potential (−0.1 V vs. RHE). Under Ar-saturated and CO_2-saturated environment, the maximum difference in total current density is 14 mA·cm^{-2} at −0.7 V vs. RHE.

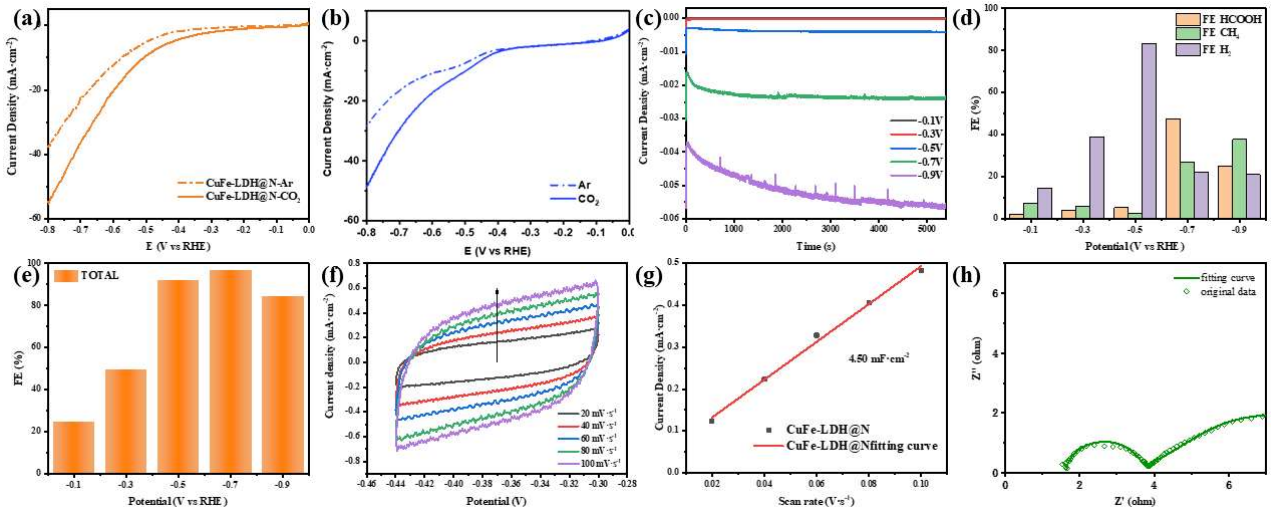

Figure 3. (a) LSV of nitrided copper-iron composite; **(b)** LSV of CuFe-LDH; **(c)** Chronoamperometry test cyclic tests; **(d-e)** the products FE of nitrided copper-iron composite at different test potentials; **(f)** Cyclic voltammograms; **(g)** Linear fit of double layer capacitance current density to scan rate from CV plot; **(g)** The Nyquist plots.

The main product of electrocatalytic CO_2RR over the catalyst is the C_1 product including HCOOH and CH_4, the faradaic efficiency (FE) of HCOOH and CH_4 is 47.55% and 27.13% respectively with the maximum FE of 96.77 % at −0.7 V vs. RHE (**Figures 3d** and **3e**). In particular, at −0.7 V, the partial current densities of HCOOH and CH_4 are 17.29 mA cm^{-2} and 9.8 mA cm^{-2}, respectively. However, only a tiny amount of HCOOH is produced due to CO_2 reduction by CuFe-LDH precursor (**Figure A4**). Compared with the literature, it becomes evident that the FE of C_1 products achieved by the catalyst in this study exceeds that of numerous copper-based catalysts (**Table 1**). During the electroreduction of CO_2, the cationic reduction produced by the catalyst consumes part of the charge, resulting in a total FE of the obtained product of less than 100%. To confirm the electrochemical stability of nitrided copper-iron composite oxide, cycling tests were carried out for 10 h at the optimum potential of −0.7 V (**Figure A5**). The results show that the FE of CH_4 decreased slightly, indicating that this catalyst has good electrochemical stability. As revealed in **Figure A6**, the XPS spectra of the catalyst after cycling tests show no obvious change in the valence state or proportion of surface elements, further confirming the excellent stability of the material.

In addition, the high surface area and fast electron transport kinetics of nitrided copper-iron composite oxide were confirmed by electrochemical active area (ECSA) and electrochemical impedance spectroscopy (EIS). As shown in **Figures 3f** and **3g**, the ECSA value of nitrided copper-iron composite oxide (C_{dl} = 4.50 mF·cm^{-1}) is 3 times that of CuFe-LDH (C_{dl} = 1.53 mF·cm^{-1}) (**Figure A7**). The Nyquist diagram in **Figure 3h** shows that the semicircle diameter (charge transfer resistance, 1.8 Ω) of nitrided copper-iron composite oxide at operating voltage is also smaller than that of CuFe-LDH (2.6 Ω). The above results indicate that the kinetic performance of the obtained catalyst through nitridation surpasses that of its precursor.

Table 1. Comparison of the electrocatalytic activity of catalyst in this work with other catalysts for electrochemical reduction of CO_2.

Catalysts	Concentration of electrolyte	Main products	Potential at FE_{max} (V vs. RHE)	Selectivity FE (%)	*J* (mA·cm^{-2})	References
Cu_3PdxN	0.5M $KHCO_3$	CH_4	−1.25	49.7	8.6	[52]
CuO–P NW	0.1 M KCl	CH_4	−1.1	34	3.5	[53]
Cu-PTI	0.5M $KHCO_3$	CH_4	−0.84	68	236.0	[54]
Cu/Au	0.1M $NaHCO_3$	CH_4	−0.7	16	-	[55]
Cu (II)	1 M KOH	CH_4	−1.0	42	100.0	[56]
ESGDE	0.5M $KHCO_3$	HCOOH	−1.16	73	34.0	[57]
Cu foam	0.1 M $KHCO_3$	HCOOH	−1.3	48	1.0	[58]
Nitrided copper-iron composite	0.5M $KHCO_3$	HCOOH; CH_4	−0.7	47.5; 27.1	17.2; 9.8	This work

3.3. Mechanisms of CH_4 and HCOOH formation

The catalysts underwent chronoamperometric tests at different potentials for 1000 s with the intention of investigating the reaction mechanism and active sites of the catalyst. The SEM images of nitrided copper-iron composite oxide after CO_2

reduction test at −0.10, −0.30, −0.50, −0.70 and −0.90 V are shown in **Figure A8**. The structure of the nitrided catalyst has shown a transition from particles to agglomerates during CO_2 electroreduction.

The existence state of surface elements of the catalyst after chronoamperometric tests at potentials of −0.10, −0.30, −0.50, −0.70 and −0.90 V were analyzed by XPS. (**Figures 4a** and **4b**). The Cu atoms in the catalyst were shown to be mainly Cu^+ and Cu^{2+} during the reaction. In Cu 2p XPS spectra, peaks at 935.19 eV and 955.01 eV are attributed to Cu^{2+}, and peaks at 932.37 eV and 953.38 eV are attributed to Cu^0 or Cu^+ (**Figure 4a**). The precise state of Cu was further identified by AES (**Figure 4b**), there is a peak assigned to Cu^+ in the Cu LMM spectrum of nitrided copper-iron composite oxide, but no peak attributed Cu^+ appeared [59,60]. The Cu^+/Cu^{2+} ratio decreases and then increases with increasing potential as the potential increases from −0.1 V vs. RHE to −0.9 V vs. RHE (**Table S1**). This is the same trend as the total FE. This result indicates that Cu^+ is converted to Cu^{2+} during the reaction process. Therefore, it is believed that the reaction process involves the loss of electrons from Cu^+ as the active site to activate CO_2. Different from Cu, the existence state of Fe remained relatively unchanged, indicated by the lack of significant differences in the integrated XPS area when compared to the un-reacted state (**Figure A9**). The overlapping of the $2P_{1/2}$ and $2P_{3/2}$ peaks of Fe could be due to the interference of the LMM spectrum of Cu. This provides further evidence for the excellent stability of the catalyst.

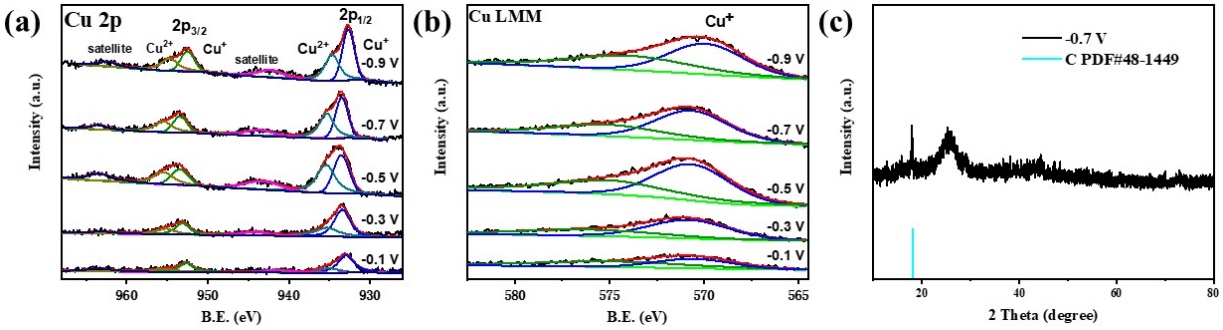

Figure 4. (a) XPS spectra of Cu 2p; **(b)** Cu LMM; **(c)** XRD of material and substrate after the reaction.

To investigate the reaction mechanism in detail, in situ ATR-FTIR was used to detect the intermediates formation during CO_2 electroreduction (**Figure 5**). The peak at about 2400 cm^{-1} belongs to the stretching vibration of Stretching Vibration of CO_2. The peak of the stretching vibration of *COOH appears in the resonant band at around 1490 cm^{-1}. (* represents the adsorption state). The vibrational peaks of desorbed *CO, bridged *CO, and linear adsorbed *CO should appear at the resonance band of about 2100–2000 cm^{-1}. However, no corresponding signal was detected, possibly due to the high reactivity of *CO during the reaction process. The *CO readily reacts with protons to form *CHO for the following reaction, as indicated by the signals of the *CHO vibrational stretching peaks at 1046 cm^{-1}.

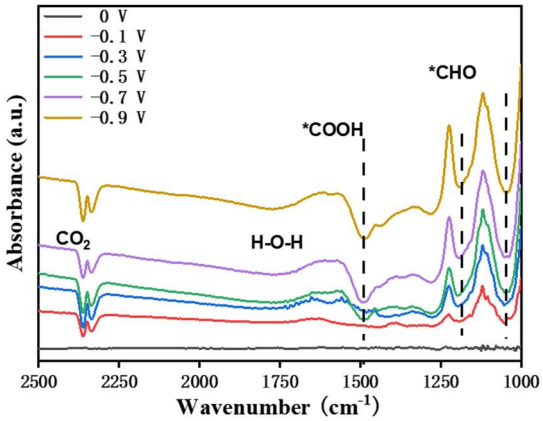

Figure 5. In-situ ATR-FTIR of CO_2 reduction on nitrided copper-iron composite oxides during CO_2 reduction LSV tests with different potentials.

Based on the above analysis, the CO_2 reduction path was proposed as follows (**Figure 6**). During the CO_2 reduction process, amorphous nitrided copper-iron composite oxides adsorb CO_2 first, and then CO_2 is converted into *COOH through proton-electron coupling. The conversion of *COOH has two pathways: Part of *COOH directly combines with protons in the solution, forming the HCOOH product. The other part of *COOH undergoes the process of proton dehydration addition, forming the *CO intermediate. The unclear *CO signal suggests that it rapidly proceeds to the subsequent reaction step, combining protons in solution to form *CHO. *CHO then combines with protons and undergoes dehydration to form CH_4, which is more challenging to carry out compared to the first step, resulting in a lower FE of CH_4 than HCOOH at different potentials. The e^- during the reaction is supplied by the active site Cu^+.

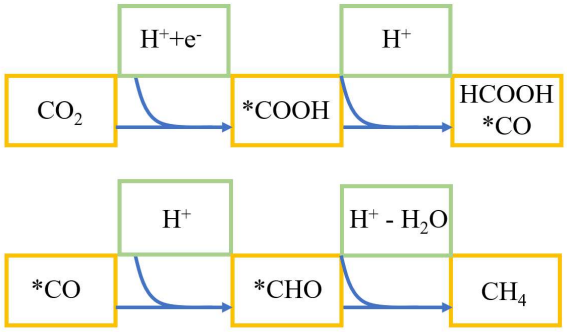

Figure 6. Mechanism of nitrided copper-iron composite oxides electro-catalyze CO_2RR reaction.

4. Conclusion and outlook

The nitrided copper-iron composite nanocomposites were synthesized by urea nitridation of CuFe-LDH precursor at high temperature. The obtained catalyst has low production cost and exhibits good electrocatalytic CO_2RR performance. The nitrided copper-iron composite FE was 47.55 % for HCOOH and 27.13 % for CH_4 at −0.7 V, achieving a total FE of 96.77 %. The performance of the catalyst remained stability after 10 h of continuous testing with the FE of CH_4 product remaining stable above 27 % at −0.7 V and the structure also remaining stable. In situ ATR-FTIR studies show

that the existence of Cu^+ sites can furnish electrons to *CHO. This study demonstrates the potential of amorphous copper iron oxide nitride as a catalyst for CO_2 electroreduction, and provides new ideas for the design of efficient catalysts. But amorphous materials face several major challenges as catalysts in the CO_2RR. Firstly, amorphous materials may have multiple active sites, which may lead to competition for multiple reaction pathways and products, thus reducing the selectivity of the target product. Secondly, amorphous materials are often more complex to prepare than crystalline materials, and their characterization methods are more limited. This may limit an in-depth understanding of the structure and properties of the materials. Amorphous oxide electrocatalysts should be studied more thoroughly using more advanced characterization tools to understand their microstructures (e.g., defects), active sites, and electrocatalytic processes, which will help to design amorphous oxides with desirable electrocatalytic properties.

5. Supporting information

Additional tables and figures for characterization of the synthesized materials' morphology and composition include SEM images of CuFe-LDH, the EDS spectrum of nitrided copper-iron composite nanocomposites, CO_2 electroreduction activity of CuFe-LDH, stability test results, SEM images of nitrided copper-iron composite oxide after the chronoamperometric i-t tests at different potentials, Nyquist plots of CuFe-LDH and nitrided copper-iron composite oxide, XPS spectra of Fe 2p of nitrided copper-iron composite, and ratios of Cu^+, Cu^{2+}, and Cu^+/Cu^{2+} calculated by Cu 2p spectra of nitrided copper-iron composite oxide.

Author contributions: Conceptualization, XL; methodology, DS and JH; software, validation, XZ, XL, FZ and YW; formal analysis, DS; investigation, JH; resources, XL; data curation, DS; writing—original draft preparation, DS; writing—review and editing, XL and YW; visualization, supervision, XL and YW; project administration, funding acquisition, XL. All authors have read and agreed to the published version of the manuscript.

Acknowledgments: This research was funded by the National Natural Science Foundation of China (Nos.22278020), the Fundamental Research Funds for the Central Universities (Nos. 12060093063 and XK1803-05), and the Program for Changjiang Scholars and Innovative Research Teams in University (No. IRT1205).

Conflict of interest: The authors declare no conflict of interest.

References

1. Birdja YY, Pérez-Gallent E, Figueiredo MC, et al. Advances and challenges in understanding the electrocatalytic conversion of carbon dioxide to fuels. Nature Energy. 2019, 4(9): 732-745. doi: 10.1038/s41560-019-0450-y
2. Zhang Y, Guo SX, Zhang X, et al. Mechanistic understanding of the electrocatalytic CO_2 reduction reaction – New developments based on advanced instrumental techniques. Nano Today. 2020, 31: 100835. doi: 10.1016/j.nantod.2019.100835
3. Chernyak SA, Ivanov AS, Maksimov SV, et al. Fischer-Tropsch synthesis over carbon-encapsulated cobalt and iron nanoparticles embedded in 3D-framework of carbon nanotubes. Journal of Catalysis. 2020, 389: 270-284. doi: 10.1016/j.jcat.2020.06.011

4. Gong W, Ye RP, Ding J, et al. Effect of copper on highly effective Fe-Mn based catalysts during production of light olefins via Fischer-Tropsch process with low CO_2 emission. Applied Catalysis B: Environmental. 2020, 278: 119302. doi: 10.1016/j.apcatb.2020.119302
5. Nitopi S, Bertheussen E, Scott SB, et al. Progress and Perspectives of Electrochemical CO_2 Reduction on Copper in Aqueous Electrolyte. Chemical Reviews. 2019, 119(12): 7610-7672. doi: 10.1021/acs.chemrev.8b00705
6. Ding P, Zhao H, Li T, et al. Metal-based electrocatalytic conversion of CO_2 to formic acid/formate. Journal of Materials Chemistry A. 2020, 8(42), 21947-21960. doi: 10.1039/D0TA08393C.
7. Xu C, Dong Y, Zhao H, et al. CO_2 Conversion Toward Real-World Applications: Electrocatalysis versus CO_2 Batteries. Advanced Functional Materials. 2023, 33(32). doi: 10.1002/adfm.202300926
8. Plankensteiner N, Rondou N, Blom MJW, et al. Competitive enhancement of CO_2 reduction reactions versus hydrogen evolution for high surface area electrodes: A comparative study for Cu and Ag nanomesh. Electrochimica Acta. 2024, 474: 143495. doi: 10.1016/j.electacta.2023.143495
9. Pourebrahimi S, Pirooz M, Ahmadi S, et al. Nanoengineering of metal-based electrocatalysts for carbon dioxide (CO_2) reduction: A critical review. Materials Today Physics. 2023, 38: 101250. doi: 10.1016/j.mtphys.2023.101250
10. Nielsen DU, Hu XM, Daasbjerg K, et al. Chemically and electrochemically catalysed conversion of CO_2 to CO with follow-up utilization to value-added chemicals. Nature Catalysis. 2018, 1(4): 244-254. doi: 10.1038/s41929-018-0051-3
11. Xu F, Wu D, Wang Z, et al. Synergistic effect and high performance of transition metal-anchored boron-doped graphyne electrocatalyst applied in the electroreduction of CO_2 to C_1 products: A DFT study. Applied Surface Science. 2023, 631: 157505. doi: 10.1016/j.apsusc.2023.157505
12. Peterson AA, Abild-Pedersen F, Studt F, et al. How copper catalyzes the electroreduction of carbon dioxide into hydrocarbon fuels. Energy & Environmental Science. 2010, 3(9): 1311. doi: 10.1039/c0ee00071j
13. Oloman C, Li H. Electrochemical Processing of Carbon Dioxide. ChemSusChem. 2008, 1(5): 385-391. doi: 10.1002/cssc.200800015
14. Hori Y. Electrochemical CO_2 Reduction on Metal Electrodes. In: Vayenas CG, White RE, Gamboa-Aldeco ME (editors). Modern Aspects of Electrochemistry. Springer; 2008. pp. 89-189.
15. Wei L, Meng D, Jiang Q, et al. A review on oxygen evolution electrocatalysts based on the different Ni-Fe matrix composites. Journal of Environmental Chemical Engineering. 2022, 10(6): 108591. doi: 10.1016/j.jece.2022.108591
16. Pan F, Li B, Sarnello E, et al. Pore-Edge Tailoring of Single-Atom Iron–Nitrogen Sites on Graphene for Enhanced CO_2 Reduction. ACS Catalysis. 2020, 10(19): 10803-10811. doi: 10.1021/acscatal.0c02499
17. Su J, Pan D, Dong Y, et al. Ultrafine Fe_2C Iron Carbide Nanoclusters Trapped in Topological Carbon Defects for Efficient Electroreduction of Carbon Dioxide. Advanced Energy Materials. 2023, 13(20). doi: 10.1002/aenm.202204391
18. He J, Hu B, Zhao Y. Superaerophobic Electrode with Metal@Metal-Oxide Powder Catalyst for Oxygen Evolution Reaction. Advanced Functional Materials. 2016, 26(33): 5998-6004. doi: 10.1002/adfm.201602116
19. Wei X, Wei S, Cao S, et al. Cu acting as Fe activity promoter in dual-atom Cu/Fe-NC catalyst in CO_2RR to C_1 products. Applied Surface Science. 2021, 564: 150423. doi: 10.1016/j.apsusc.2021.150423
20. Bagger A, Ju W, Varela AS, et al. Electrochemical CO_2 Reduction: Classifying Cu Facets. ACS Catalysis. 2019, 9(9): 7894-7899. doi: 10.1021/acscatal.9b01899
21. Cometto C, Ugolotti A, Grazietti E, et al. Copper single-atoms embedded in 2D graphitic carbon nitride for the CO_2 reduction. npj 2D Materials and Applications. 2021, 5(1). doi: 10.1038/s41699-021-00243-y
22. Kong Q, An X, Liu Q, et al. Copper-based catalysts for the electrochemical reduction of carbon dioxide: progress and future prospects. Materials Horizons. 2023, 10(3): 698-721. doi: 10.1039/d2mh01218a
23. Yu P, Lv X, Wang Q, et al. Promoting Electrocatalytic CO_2 Reduction to CH_4 by Copper Porphyrin with Donor–Acceptor Structures. Small. 2022, 19(4). doi: 10.1002/smll.202205730
24. Yang YL, Wang YR, Gao GK, et al. Self-assembly of single metal sites embedded covalent organic frameworks into multi-dimensional nanostructures for efficient CO_2 electroreduction. Chinese Chemical Letters. 2022, 33(3): 1439-1444. doi: 10.1016/j.cclet.2021.08.063
25. Liu B, Peng H, Cheng J, et al. Nitrogen-Doped Graphene-Encapsulated Nickel–Copper Alloy Nanoflower for Highly Efficient Electrochemical Hydrogen Evolution Reaction. Small. 2019, 15(48). doi: 10.1002/smll.201901545
26. Portha JF, Parkhomenko K, Kobl K, et al. Kinetics of Methanol Synthesis from Carbon Dioxide Hydrogenation over Copper–Zinc Oxide Catalysts. Industrial & Engineering Chemistry Research. 2017, 56(45): 13133-13145. doi:

10.1021/acs.iecr.7b01323
27. Ma Y, Wang J, Yu J, et al. Surface modification of metal materials for high-performance electrocatalytic carbon dioxide reduction. Matter. 2021, 4(3): 888-926. doi: 10.1016/j.matt.2021.01.007
28. Bui TS, Lovell EC, Daiyan R, et al. Defective Metal Oxides: Lessons from CO_2RR and Applications in NO_XRR. Advanced Materials. 2023, 35(28). doi: 10.1002/adma.202205814
29. De Luna P, Quintero-Bermudez R, Dinh CT, et al. Catalyst electro-redeposition controls morphology and oxidation state for selective carbon dioxide reduction. Nature Catalysis. 2018, 1(2): 103-110. doi: 10.1038/s41929-017-0018-9
30. Anasori B, Lukatskaya MR, Gogotsi Y. 2D metal carbides and nitrides (MXenes) for energy storage. Nature Reviews Materials. 2017, 2(2). doi: 10.1038/natrevmats.2016.98
31. Han M, Maleski K, Shuck CE, et al. Tailoring Electronic and Optical Properties of MXenes through Forming Solid Solutions. Journal of the American Chemical Society. 2020, 142(45): 19110-19118. doi: 10.1021/jacs.0c07395
32. Xiao Y, Zhang W. High throughput screening of M_3C_2 MXenes for efficient CO_2 reduction conversion into hydrocarbon fuels. Nanoscale. 2020, 12(14): 7660-7673. doi: 10.1039/c9nr10598k
33. Li N, Chen X, Ong WJ, et al. Understanding of Electrochemical Mechanisms for CO_2 Capture and Conversion into Hydrocarbon Fuels in Transition-Metal Carbides (MXenes). ACS Nano. 2017, 11(11): 10825-10833. doi: 10.1021/acsnano.7b03738
34. Otgonbayar Z, Oh WC. MXene-based nanocomposite for the photocatalytic CO_2 reduction: Comprehensive review. Molecular Catalysis. 2023, 541: 113085. doi: 10.1016/j.mcat.2023.113085
35. Sreedhar A, Reddy IN, Noh JS. Photocatalytic and electrocatalytic reduction of CO_2 and N_2 by Ti_3C_2 MXene supported composites for a cleaner environment: A review. Journal of Cleaner Production. 2021, 328: 129647. doi: 10.1016/j.jclepro.2021.129647
36. Wang H, Li J, Li K, et al. Transition metal nitrides for electrochemical energy applications. Chemical Society Reviews. 2021, 50(2): 1354-1390. doi: 10.1039/d0cs00415d
37. Hu H, Wang X, Attfield JP, et al. Metal nitrides for seawater electrolysis. Chemical Society Reviews. 2024, 53(1): 163-203. doi: 10.1039/d3cs00717k
38. Gao B, Li X, Ding K, et al. Recent progress in nanostructured transition metal nitrides for advanced electrochemical energy storage. Journal of Materials Chemistry A. 2019, 7(1): 14-37. doi: 10.1039/c8ta05760e
39. Shan J, Sun K, Li H, et al. Composition regulation and defects introduction via amorphous CuEu alloy shell for efficient CO_2 electroreduction toward methane. Journal of CO_2 Utilization. 2020, 41: 101285. doi: 10.1016/j.jcou.2020.101285
40. Yang B, Zeng J, Zhang Z, et al. Kinetic-boosted CO_2 electroreduction to formate via synergistic electric-thermal field on hierarchical bismuth with amorphous layer. Journal of Energy Chemistry. 2024, 90: 233-243. doi: 10.1016/j.jechem.2023.11.022
41. Cao Y, Zheng D, Zhang F, et al. Layered double hydroxide (LDH) for multi-functionalized corrosion protection of metals: A review. Journal of Materials Science & Technology. 2022, 102: 232-263. doi: 10.1016/j.jmst.2021.05.078
42. Zhang J, Liu J, Xi L, et al. Single-Atom Au/NiFe Layered Double Hydroxide Electrocatalyst: Probing the Origin of Activity for Oxygen Evolution Reaction. Journal of the American Chemical Society. 2018, 140(11): 3876-3879. doi: 10.1021/jacs.8b00752
43. Zhang L, Peng J, Yuan Y, et al. Bifunctional heterostructure NiCo-layered double hydroxide nanosheets/NiCoP nanotubes/Ni foam for overall water splitting. Applied Surface Science. 2021, 557: 149831. doi: 10.1016/j.apsusc.2021.149831
44. Iwase K, Hirano T, Honma I. Copper Aluminum Layered Double Hydroxides with Different Compositions and Morphologies as Electrocatalysts for the Carbon Dioxide Reduction Reaction. ChemSusChem. 2021, 15(2). doi: 10.1002/cssc.202102340
45. Ma X, Liu T, Liu E, et al. Preparation and performance of Cd-MgAl-LDHs@RGO in high efficiency electrocatalytic reduction of CO_2 to CO. Molecular Catalysis. 2023, 535: 112876. doi: 10.1016/j.mcat.2022.112876
46. Zhang ZY, Tian H, Bian L, et al. Cu-Zn-based alloy/oxide interfaces for enhanced electroreduction of CO_2 to C^{2+} products. Journal of Energy Chemistry. 2023, 83: 90-97. doi: 10.1016/j.jechem.2023.04.034
47. He J, Dou T, Diao S, et al. Cu/Fe_3O_4 Nanocomposites from Layered Double Hydroxides as Catalysts for Selective Electroreduction of Carbon Dioxide. ACS Applied Nano Materials. 2023, 6(14): 13543-13550. doi: 10.1021/acsanm.3c02193

48. Ma Y, Chen F, Yang Q, et al. Sulfate radical induced degradation of Methyl Violet azo dye with CuFe layered doubled hydroxide as heterogeneous photoactivator of persulfate. Journal of Environmental Management. 2018, 227: 406-414. doi: 10.1016/j.jenvman.2018.08.030
49. Anantharaj S, Noda S. Amorphous Catalysts and Electrochemical Water Splitting: An Untold Story of Harmony. Small. 2019, 16(2). doi: 10.1002/smll.201905779
50. Tan BJ, Klabunde KJ, Sherwood PMA. X-ray photoelectron spectroscopy studies of solvated metal atom dispersed catalysts. Monometallic iron and bimetallic iron-cobalt particles on alumina. Chemistry of Materials. 1990, 2(2): 186-191. doi: 10.1021/cm00008a021
51. Wang WJ, Qiao MH, Yang J, et al. Selective hydrogenation of cyclopentadiene to cyclopentene over an amorphous NiB/SiO_2 catalyst. Applied Catalysis A: General. 1997, 163(1): 101-109. doi: 10.1016/S0926-860X(97)00125-7
52. Li T, Wang J, Zhu S, et al. Cu_3PdxN nanocrystals for efficient CO_2 electrochemical reduction to methane. Electrochimica Acta. 2021, 371: 137793. doi: 10.1016/j.electacta.2021.137793
53. Butt FA, Alshahrani T, Awan ZUH, et al. Electrochemical CO_2 reduction to gaseous methane and carbon monoxide using plasma-synthesized copper nanowires. Journal of Solid State Electrochemistry. 2023. doi: 10.1007/s10008-023-05600-z
54. Roy S, Li Z, Chen Z, et al. Cooperative Copper Single-Atom Catalyst in 2D Carbon Nitride for Enhanced CO_2 Electrolysis to Methane. Advanced Materials. 2024. doi: 10.1002/adma.202300713
55. Shang H, Kim D, Wallentine SK, et al. Ensemble effects in Cu/Au ultrasmall nanoparticles control the branching point for C_1 selectivity during CO_2 electroreduction. Chemical Science. 2021. doi: 10.1039/d1sc02602j
56. Zhang T, Verma S, Kim S, et al. Highly dispersed, single-site copper catalysts for the electroreduction of CO_2 to methane. Journal of Electroanalytical Chemistry. 2020, 875: 113862. doi: 10.1016/j.jelechem.2020.113862
57. Wang Q, Wang X, Wu C, et al. Electrodeposition of tin on Nafion-bonded carbon black as an active catalyst layer for efficient electroreduction of CO_2 to formic acid. Scientific Reports. 2017, 7(1). doi: 10.1038/s41598-017-14233-y
58. Ahn ST, Sen S, Palmore GTR. Grazing incidence X-Ray diffraction: identifying the dominant facet in copper foams that electrocatalyze the reduction of carbon dioxide to formate. Nanoscale. 2022, 14(36): 13132-13140. doi: 10.1039/d2nr03212k
59. Kattel S, Ramírez PJ, Chen JG, et al. Active sites for CO_2 hydrogenation to methanol on Cu/ZnO catalysts. Science. 2017, 355(6331): 1296-1299. doi: 10.1126/science.aal3573
60. El-Nagar GA, Haun F, Gupta S, et al. Unintended cation crossover influences CO_2 reduction selectivity in Cu-based zero-gap electrolysers. Nature Communications. 2023, 14(1). doi: 10.1038/s41467-023-37520-x

Appendix

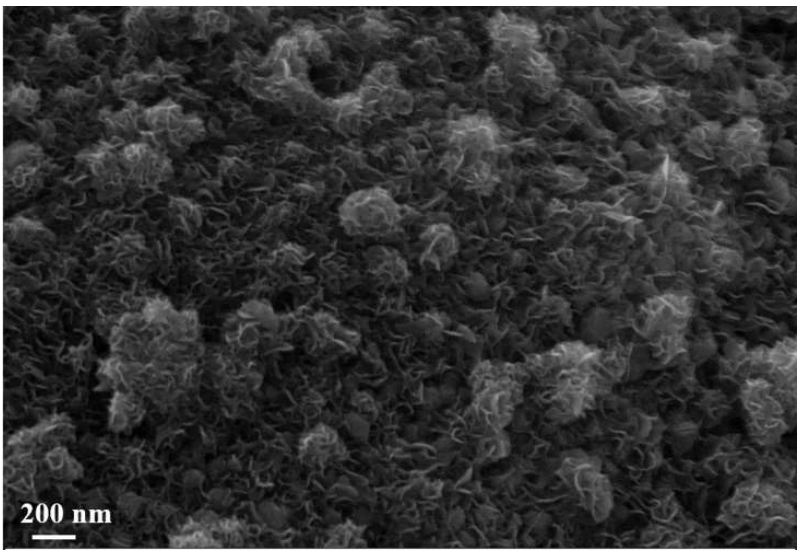

Figure A1. SEM images of $MoSe_2$.

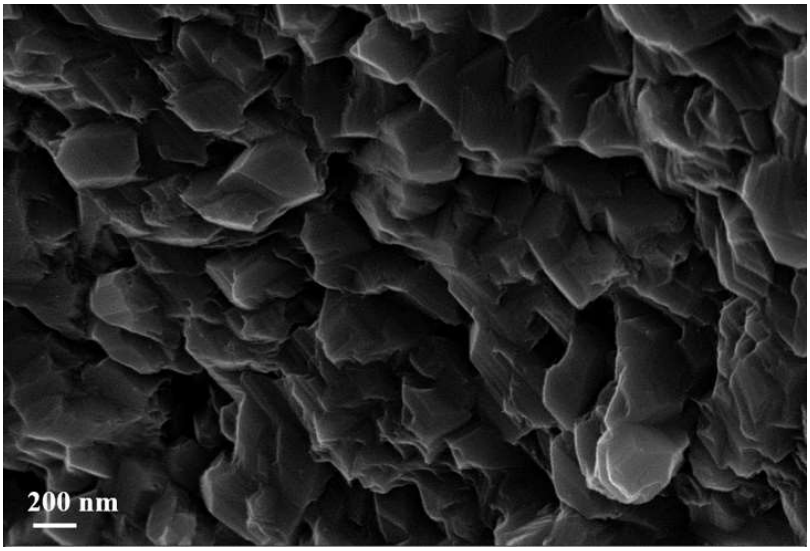

Figure A2. SEM images of $NiSe_2$.

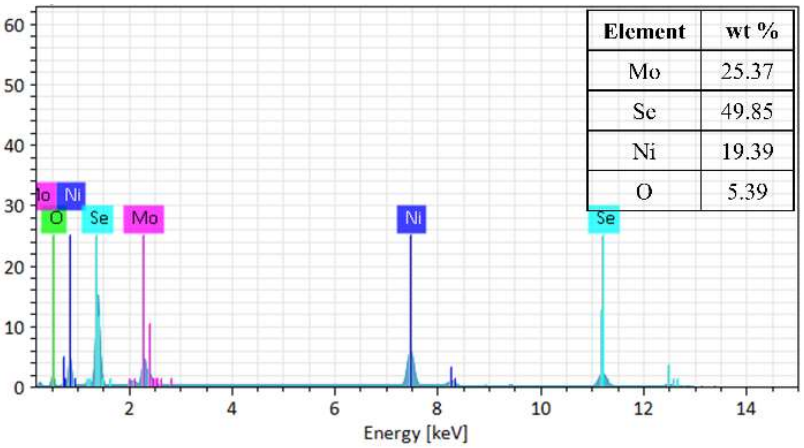

Figure A3. EDS spectrum of the $MoSe_2/NiSe_2$.

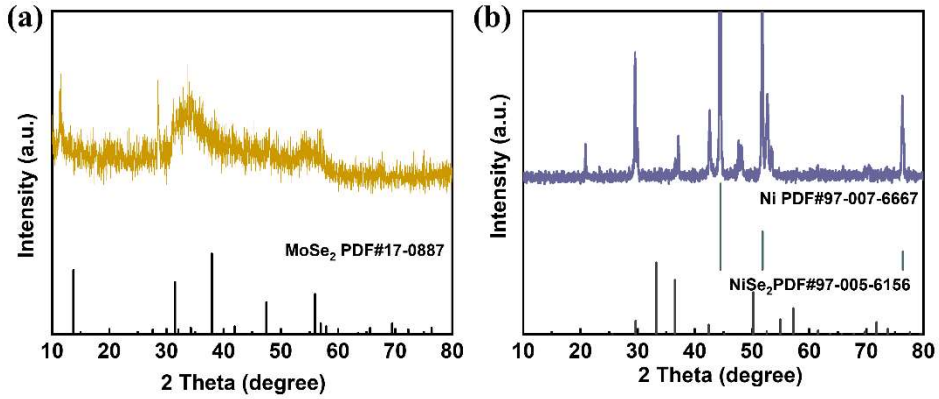

Figure A4. XRD patterns of **(a)** bare $MoSe_2$; **(b)** $NiSe_2$.

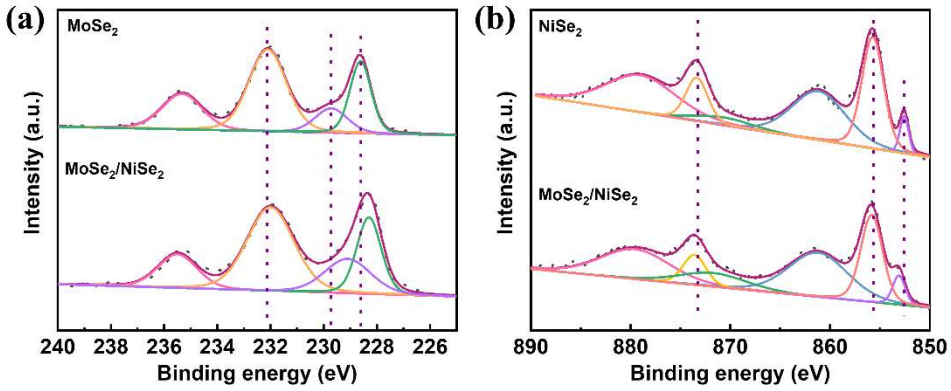

Figure A5. High-resolution XPS spectra of **(a)** Mo 3d in the $MoSe_2$ and $MoSe_2/NiSe_2$; **(b)** Ni 2p in the $NiSe_2$ and $MoSe_2/NiSe_2$.

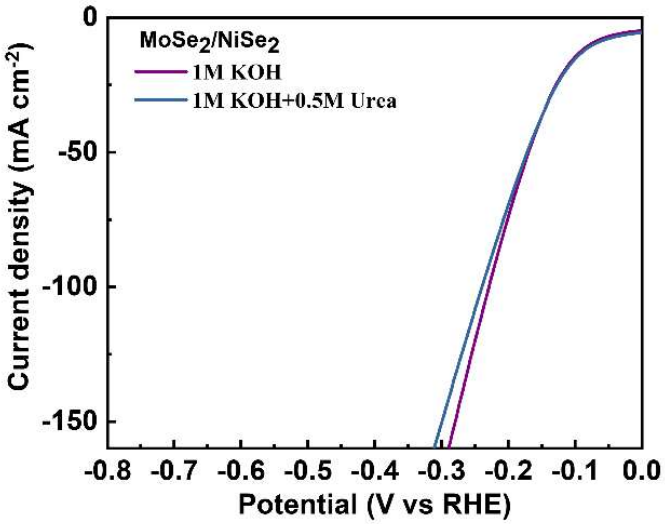

Figure A6. HER polarization plots of $MoSe_2/NiSe_2$ at a scan rate of 5 mV s^{-1} in 1 M KOH electrolyte with and without 0.5 M urea.

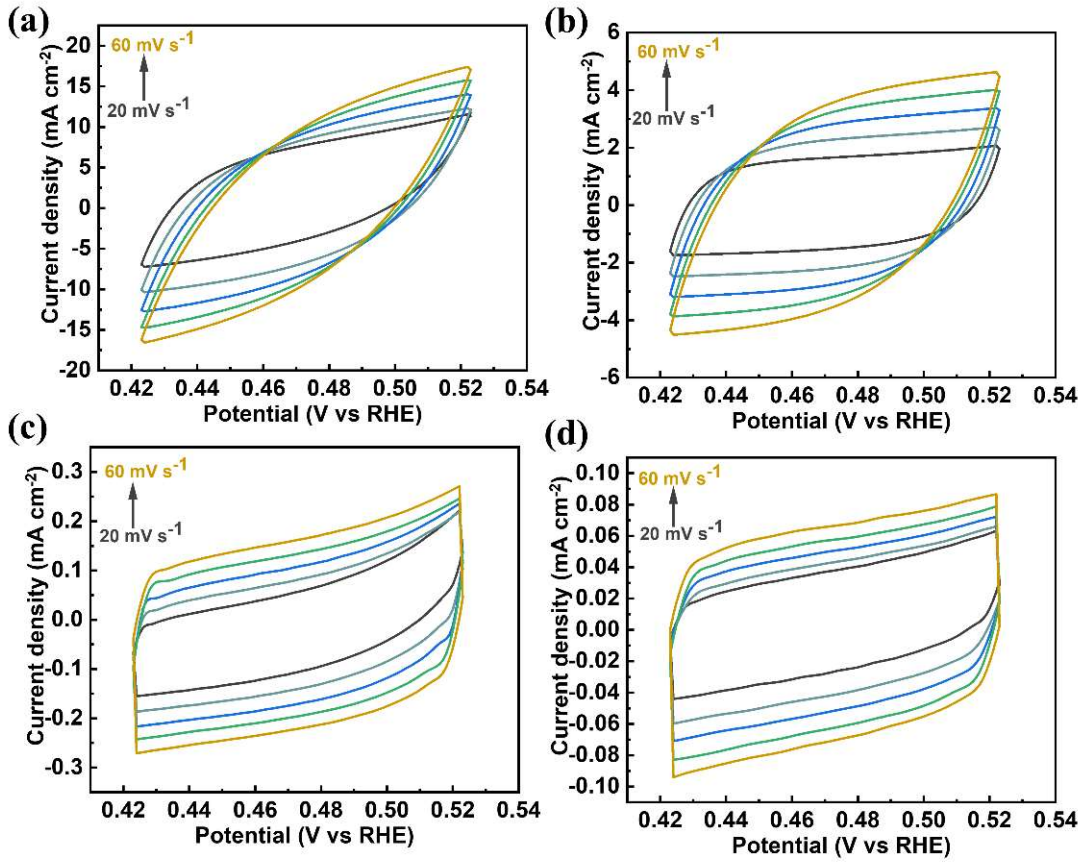

Figure A7. CV curves of **(a)** $MoSe_2/NiSe_2$; **(b)** $MoSe_2$; **(c)** $NiSe_2$; and **(d)** $NiMoO_4$/NF for HER in capacitive region at scan rates from 20 to 60 mV s^{-1} in 1 M KOH.

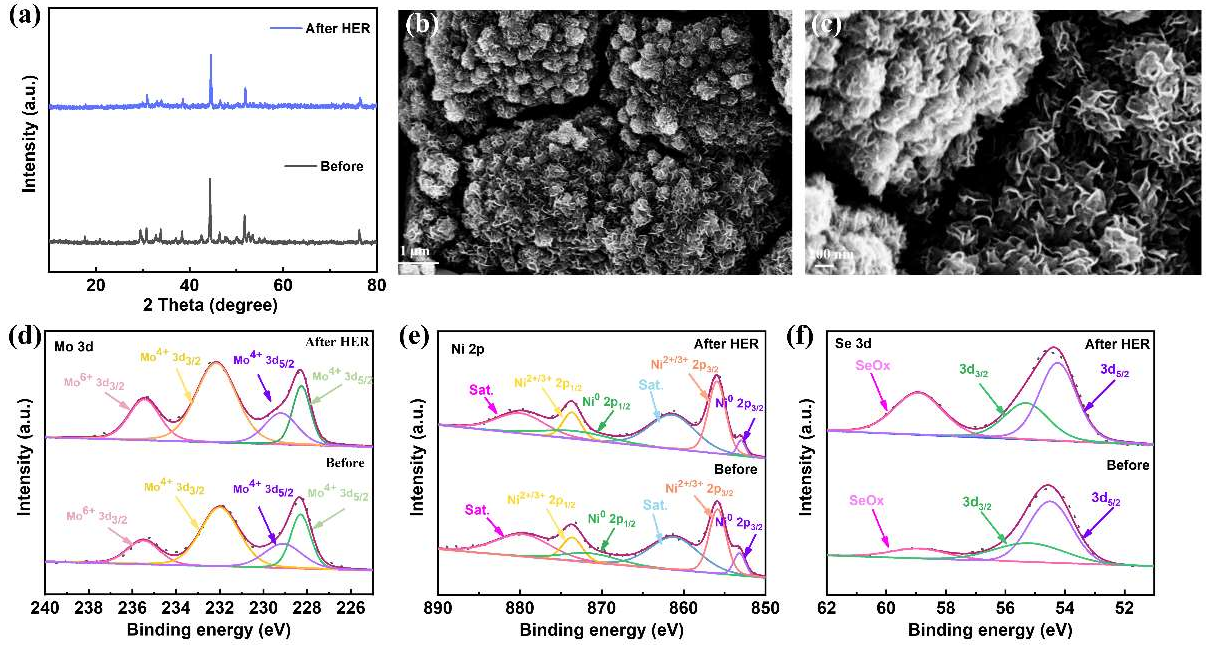

Figure A8. (a) XRD; **(b,c)** SEM images, high-resolution XPS spectra in the Mo 3d; **(d)** Ni 2p; **(e)** Se 3d; **(f)** of $MoSe_2/NiSe_2$ after HER durability test in 1M KOH.

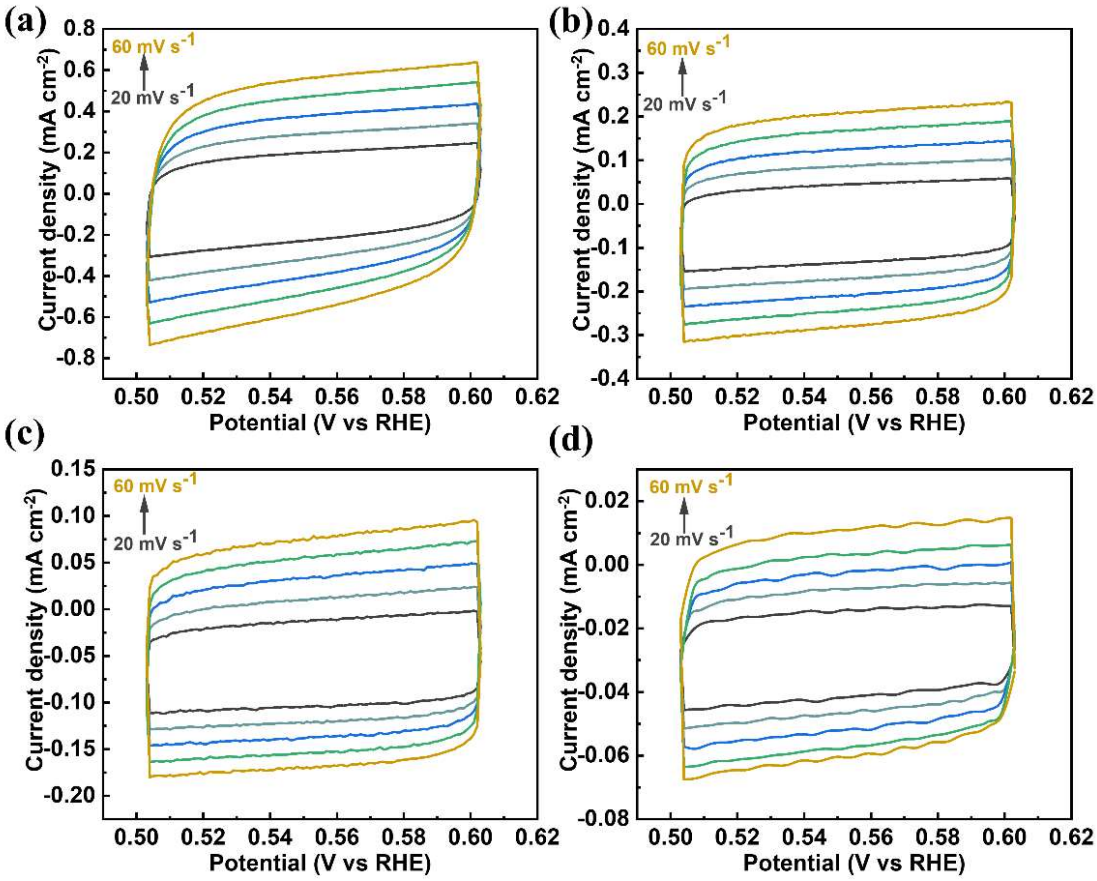

Figure A9. CV curves of **(a)** $MoSe_2/NiSe_2$; **(b)** $MoSe_2$; **(c)** $NiSe_2$; and **(d)** $NiMoO_4$/NF for UOR in capacitive region at scan rates from 20 to 60 mV s^{-1} in 1 M KOH+0.5M UOR.